

A Simultaneous Dual-Frequency Scintillation Arc Survey of Six Bright Canonical Pulsars Using the Upgraded Giant Metrewave Radio Telescope

JACOB E. TURNER,^{1,2} BHAL CHANDRA JOSHI,³ MAURA A. McLAUGHLIN,^{1,2} AND DANIEL R. STINEBRING⁴

¹*Department of Physics and Astronomy, West Virginia University, P.O. Box 6315, Morgantown, WV 26506, USA*

²*Center for Gravitational Waves and Cosmology, West Virginia University, Chestnut Ridge Research Building, Morgantown, WV 26505, USA*

³*National Centre for Radio Astrophysics, Tata Institute of Fundamental Research, Post Bag 3, Ganeshkhind, Pune - 411007, India*

⁴*Department of Physics and Astronomy, Oberlin College, Oberlin, OH 44074, USA*

ABSTRACT

We use the Upgraded Giant Metrewave Radio Telescope to measure scintillation arc properties in six bright canonical pulsars with simultaneous dual frequency coverage. These observations at frequencies from 300 to 750 MHz allowed for detailed analysis of arc evolution across frequency and epoch. We perform more robust determinations of arc curvature and scattering delay frequency-dependence than allowed by single-frequency-band-per-epoch measurements, which we find to agree with theory and previous literature. We report the discovery of a strong correlation between arc asymmetry and arc curvature, potentially indicating a link between scattering screen distance and refraction strength or the effect of asymmetric distribution of scattering material on a scattering screen. The inclusion of a 155 minute observation allowed us to resolve the scale of scintillation variations on short timescales, which we find to be directly tied to the amount of ISM sampled over the observation. Some of our pulsars showed either consistent or emerging asymmetries in arc curvature, indicating instances of refraction across their lines of sight. The presence of significant features in various pulsars, such as multiple scintillation arcs in PSR J1136+1551 and flat arclets in PSR J1509+5531, that have been found in previous works, were also sufficiently detected. Possible evidence for a timescale over which a given scattering screen dominates signal propagation was found by tracking visible scintillation arcs in each epoch in PSR J1136+1551. The interesting pulsar science accomplished with this upgraded telescope shows strong promise for important future work in pulsar astronomy.

Keywords: methods: data analysis – stars: pulsars – ISM: general – ISM: structure

1. INTRODUCTION

The scintillation of pulsar emission occurs as the result of the propagation of this emission through non-uniform distributions of free electrons in the ionized interstellar medium (IISM). This interaction results in frequency-dependent and time-evolving variations in the flux density of the pulsar signal as measured at a detector. When these variations are examined across observing frequency and time in so-called dynamic spectra, representations of the change in the pulsar signal’s intensity across frequency and time, for a given observation, they can provide valuable insight into the structure of these electron density variations along our line of sight (LOS) to a given pulsar. For observations where the scintles, bright patches in a dynamic spectrum resulting from constructive interference between photons as the result of propagation through the free electrons in the ISM, are fully resolved in frequency, have sufficient coverage in time, and exhibit structures over the course of observations including, but not limited to, non-zero slopes across frequency and time, known as scintillation drift, as well as “crisscrossing” scin-

tillation patterns, then additional information can be gained about the ISM structure along the LOS by examining the parabolic arcs, known as scintillation arcs, that can emerge by examining the Fourier transform of the dynamic spectrum (Stinebring et al. 2001). Some current hypotheses on the physical origins of these arcs postulate that they originate from compressed plasma along the boundaries of 50–100 pc size bubbles in the ISM (Stinebring et al. 2022).

Traditional measurements of scintillation arcs have typically been limited to either one observing band over all epochs (i.e., Trang & Rickett (2007)), or alternated between observing bands from epoch to epoch (i.e., Stinebring et al. (2019)). While generally sufficient for most analyses, this band limit results in a bottleneck for examining the evolution of various frequency-dependent effects over shorter timescales, including scintillation arc curvature, structures within individual arcs, and asymmetries in both arc brightness and power as a function of differential time delay. By making use of the subarray capabilities of the Upgraded Giant Metrewave Radio Telescope (uGMRT), we can effec-

tively create an ultra wideband receiver by setting multiple groups of dishes to simultaneously observe at different frequencies. This work is primarily data-focused and aims to highlight the results of some multi-frequency analyses performed on a small survey of six strong canonical pulsars using this approach. In Section 2 we discuss the data taken as part of our survey. Section 3 describes the analyses performed and the physical parameters extracted. Section 4 details the results of these analyses. Finally, Section 5 summarizes our results and discusses possible next steps.

2. DATA

Our data were taken across across eight epochs spanning MJD 58987–59497 using 22 dishes split into subarrays for simultaneous multi-frequency observations at uGMRT’s Band 3 and Band 4, centered at 400 MHz and 650 MHz, respectively, each with 200 MHz of bandwidth. This simultaneous low-frequency accessibility is comparable to instruments like CHIME that can observe continuously between 400–800 MHz and better than instruments such as the Green Bank Telescope, which, while having a wide range of low frequency coverage, can only observe below one GHz with at most 240 MHz of bandwidth at frequencies close to one GHz and less than 200 MHz of bandwidth in lower frequency ranges. Observations were also made at Band 5 centered at 1360 MHz, although due to a combination of RFI and low S/N no scintles were detectable in the dynamic spectra. The observing bands were split into 4096 49 kHz wide frequency channels and observed with 10 second subintegrations. These data were flux calibrated using observations of either 3C147 or 3C286 taken at the beginning of every observing session and every pulsar was phase calibrated with a nearby source for five minutes once every 40 minutes of observing time on the pulsar. Two to three pulsars were observed at each epoch for 40 minutes each, except for MJD 59497, where three pulsars were observed for 155 minutes each. As a result of the phase calibration, each of those observations were comprised of three 40 minute sub-observations plus an additional 20 minute sub-observation.

3. ANALYSIS

All observations were processed to extract their dynamic spectra by calculating the intensity, S , of the pulsar’s signal at each observing frequency, ν , and time, t , via

$$S(\nu, t) = \frac{P_{\text{on}}(\nu, t) - P_{\text{off}}(\nu, t)}{P_{\text{bandpass}}(\nu, t)}, \quad (1)$$

where P_{bandpass} is the total power of the observation as a function of observing frequency and time, and P_{on} and P_{off} are the power in all on- and off-pulse components, respectively, as a function of frequency and time. Each dynamic

spectrum was then broken up into four 50 MHz spectra to allow for more in-depth frequency-dependent analyses and manually zapped by examining dynamic spectra data arrays and removing pixels that were brighter than the brightest scintle maxima. Secondary spectra were then created by taking the absolute square of the Fourier transform (i.e., the power spectrum) of the corresponding dynamic spectrum and converting it to units of dB. The primary (brightest) scintillation arcs on the positive and negative side of each secondary spectrum’s fringe frequency axis were then found via separate $f_\nu = \eta f_t^2$ fits, where f_ν is the differential time delay, η is the arc curvature, and f_t is the fringe frequency.

We also determined scintillation parameters by using the python package Pypulse (Lam 2017) to create the 2D autocorrelation functions (ACFs) of each dynamic spectrum and fit 2D Gaussians to these ACFs to determine their scintillation bandwidth, $\Delta\nu_d$, defined as the half-width at half-maximum (HWHM) along the frequency axis of the ACF at lag 0, scintillation timescale, Δt_d , defined as the half-width at e^{-1} along the time axis at ACF lag 0, and scintillation drift rate, $d\nu/dt$, defined as the rotation of the 2D Gaussian fit to the 2D ACF in the plane of the frequency and time lags. For our scattering delay scaling index analysis, our measured scintillation bandwidths were converted to scattering delays using

$$2\pi\Delta\nu_d\tau = C_1, \quad (2)$$

where C_1 is a dimensionless quantity between 0.6 – 1.5 that depends on the spectrum of the electron density fluctuations and geometry of the medium (Cordes & Rickett 1998). For this work we use $C_1 = 1$.

4. RESULTS & DISCUSSION

Measured arc curvatures and their corresponding dynamic spectrum scintillation drift rates can be found in Table 1. All curvatures and their uncertainties have been scaled to their corresponding value at 1 GHz assuming a ν^{-2} frequency dependence (Hill et al. 2003). Here errors on the arc curvatures represent fitting errors from the linear least squares fit. Some pulsars on MJD 59497 have multiple curvature measurements at a given frequency, which is the result of this epoch being 155 minutes instead of the 40 minutes of the other observations. As a result, a new η was measured after every 40 minutes since these observations were broken up into 40 minute chunks separated by five minute phase calibrations. On days where measurements are given for the left or right arm only, arcs on the other side of the fringe frequency axis may have been present, but were unmeasurable due to either having insufficient extension along the differential delay axis, insufficient flux relative to the background noise, being too diffuse, being too close to central spike in flux that commonly occurs around a fringe frequency of 0 mHz, or some combination of these factors.

Table 1. Pulsar Scintillation Arc Curvatures and Drift Rates

Pulsar	MJD	Frequency (MHz)	η_L (s ³)	σ_{η_L} (s ³)	η_R (s ³)	σ_{η_R} (s ³)	$d\nu/dt$ (MHz/min)	$\sigma_{d\nu/dt}$ (MHz/min)
J0630-2834	58987	325	—	—	0.2071	0.0069	-0.0164	0.0009
J0630-2834	58987	375	—	—	0.2331	0.0160	-0.0676	0.0097
J0630-2834	58987	425	—	—	0.2932	0.0223	-0.0343	0.0027
J0630-2834	58987	475	—	—	0.2037	0.0207	-0.0574	0.0059
J0630-2834	58987	575	—	—	0.1220	0.0061	0.0076	0.0025
J0630-2834	58987	625	—	—	0.1233	0.0049	-0.0779	0.0097
J0630-2834	58987	675	—	—	0.1553	0.0058	0.0818	0.0118
J0630-2834	58987	725	—	—	0.2566	0.0162	0.2685	0.0196
J1136+1551	58987	325	0.0154	0.0007	0.0238	0.0006	—	—
J1136+1551	58987	375	0.0198	0.0009	0.0231	0.0005	0.0202	0.0067
J1136+1551	58987	425	0.0195	0.0010	0.0225	0.0004	-0.0287	0.0074
J1136+1551	58987	575	0.0214	0.0005	0.0218	0.0003	-0.0173	0.0067
J1136+1551	58987	625	0.0202	0.0007	0.0229	0.0002	—	—
J1136+1551	58987	675	0.0199	0.0005	0.0249	0.0003	-0.0322	0.0250
J1136+1551	58987	725	0.0203	0.0007	0.0282	0.0006	0.00004	0.7446
J1136+1551	58991	325	0.0126	0.0004	0.0234	0.0005	0.0048	0.0093
J1136+1551	58991	375	0.0149	0.0007	0.0253	0.0007	0.2686	0.0128
J1136+1551	58991	425	0.0167	0.0009	0.0250	0.0006	—	—
J1136+1551	58991	475	0.0183	0.0007	0.0225	0.0005	-0.0402	0.0123
J1136+1551	58991	575	0.0165	0.0005	0.0254	0.0005	0.0097	0.0026
J1136+1551	58991	625	0.0178	0.0008	0.0271	0.0005	-0.0088	0.0034
J1136+1551	58991	675	0.0173	0.0007	0.0261	0.0004	—	—
J1136+1551	58991	725	0.0171	0.0007	0.0239	0.0003	0.00003	0.4211
J1136+1551	59115	325	0.0084	0.0002	0.0099	0.0002	0.2219	0.0095
J1136+1551	59115	375	0.0085	0.0003	0.0116	0.0003	0.1232	0.0115
J1136+1551	59115	425	0.0095	0.0005	0.0139	0.0004	—	—
J1136+1551	59115	475	0.0092	0.0005	0.0129	0.0004	0.0869	0.0079
J1136+1551	59115	575	0.0095	0.0003	0.0111	0.0002	0.0057	0.0014
J1136+1551	59115	625	0.0135	0.0007	0.0141	0.0006	—	—
J1136+1551	59115	675	0.0143	0.0004	0.0154	0.0003	0.0159	0.0057
J1136+1551	59115	725	0.0130	0.0005	0.0160	0.0005	0.0109	0.0036
J1136+1551	59497	325	0.0065	0.0002	0.0070	0.0003	-0.1251	0.0104
J1136+1551	59497	375	0.0078	0.0004	0.0077	0.0005	-0.0554	0.0069
J1136+1551	59497	425	0.0079	0.0002	0.0072	0.0002	-0.0119	0.0019
J1136+1551	59497	475	0.0070	0.0003	0.0068	0.0004	-0.0293	0.0044
J1136+1551	59497	325	0.0070	0.0001	0.0067	0.0002	0.0076	0.0030
J1136+1551	59497	375	0.0077	0.0002	0.0068	0.0002	0.2637	0.0498
J1136+1551	59497	425	0.0072	0.0002	0.0076	0.0002	-0.0544	0.0066

Table 1 continued

Table 1 (*continued*)

Pulsar	MJD	Frequency	η_L	σ_{η_L}	η_R	σ_{η_R}	$d\nu/dt$	$\sigma_{d\nu/dt}$
		(MHz)	(s ³)	(s ³)	(s ³)	(s ³)	(MHz/min)	(MHz/min)
J1136+1551	59497	475	0.0069	0.0001	0.0067	0.0002	-0.0302	0.0045
J1136+1551	59497	325	0.0075	0.0002	0.0075	0.0002	-0.0651	0.0058
J1136+1551	59497	375	0.0076	0.0002	0.0076	0.0003	-0.0877	0.0175
J1136+1551	59497	425	0.0082	0.0002	0.0075	0.0002	-0.0656	0.0064
J1136+1551	59497	475	0.0067	0.0002	0.0074	0.0003	-0.0417	0.0053
J1136+1551	59497	575	0.0063	0.0004	0.0079	0.0013	-0.0977	0.0507
J1136+1551	59497	675	0.0059	0.0004	0.0075	0.0007	—	—
J1136+1551	59497	725	0.0057	0.0005	0.0068	0.0008	—	—
J1509+5531	58987	575	0.3155	0.0191	0.1798	0.0063	—	—
J1509+5531	58987	625	0.3642	0.0184	0.2021	0.0060	-0.0284	0.0224
J1509+5531	58987	675	0.3410	0.0207	0.1978	0.0078	-1.5130	0.0117
J1509+5531	59064	575	0.2611	0.0147	0.2495	0.0116	0.0015	0.0030
J1509+5531	59064	625	0.2890	0.0170	0.2767	0.0118	—	—
J1509+5531	59064	675	0.2736	0.0181	0.2714	0.0128	0.0039	0.0016
J1509+5531	59064	725	0.2921	0.0186	0.2930	0.0142	0.1192	0.0728
J1509+5531	59115	575	0.0852	0.0029	0.0928	0.0037	—	—
J1509+5531	59115	625	0.0868	0.0029	0.0964	0.0044	0.0173	0.0066
J1509+5531	59115	675	0.0958	0.0031	0.0908	0.0044	-0.0970	0.0628
J1509+5531	59115	725	0.1074	0.0026	0.0872	0.0030	—	—
J1509+5531	59497	575	0.0992	0.0034	0.1139	0.0045	-0.9922	0.0226
J1509+5531	59497	625	0.1057	0.0032	0.1257	0.0043	0.0186	0.0140
J1509+5531	59497	675	0.1088	0.0033	0.1160	0.0035	—	—
J1509+5531	59497	725	0.0973	0.0026	0.1337	0.0036	0.0517	0.0395
J1509+5531	59497	575	0.0706	0.0028	0.1054	0.0047	—	—
J1509+5531	59497	625	0.0741	0.0026	0.1101	0.0046	0.0059	0.0047
J1509+5531	59497	675	0.0782	0.0022	0.1200	0.0047	0.0109	0.0086
J1509+5531	59497	725	0.0808	0.0021	0.1265	0.0040	—	—
J1509+5531	59497	675	0.0606	0.0020	0.1194	0.0042	—	—
J1645-0317	59074	575	0.0832	0.0051	—	—	0.2015	0.0091
J1645-0317	59074	625	0.0885	0.0059	—	—	-0.1688	0.0098
J1645-0317	59074	675	0.0806	0.0063	—	—	-0.1812	0.0091
J1645-0317	59074	725	0.0832	0.0061	—	—	-0.2235	0.0105
J1932+1059	58997	325	0.0382	0.0030	0.0331	0.0018	-0.1092	0.0227
J1932+1059	58997	375	0.0358	0.0016	0.0364	0.0020	—	—
J1932+1059	58997	425	0.0346	0.0006	0.0335	0.0007	-0.0224	0.0086
J1932+1059	58997	475	0.0365	0.0007	0.0335	0.0005	0.1987	0.0427
J1932+1059	58997	575	0.0351	0.0005	0.0360	0.0004	0.0181	0.0093
J1932+1059	58997	625	0.0366	0.0005	0.0335	0.0004	0.0614	0.0352
J1932+1059	58997	675	0.0359	0.0010	0.0358	0.0010	-0.0062	0.0016
J1932+1059	58997	725	0.0373	0.0007	0.0348	0.0012	-0.0074	0.0022

Table 1 (*continued*)

Table 1 (*continued*)

Pulsar	MJD	Frequency (MHz)	η_L (s ³)	σ_{η_L} (s ³)	η_R (s ³)	σ_{η_R} (s ³)	$d\nu/dt$ (MHz/min)	$\sigma_{d\nu/dt}$ (MHz/min)
J1932+1059	59062	325	0.0330	0.0006	0.0271	0.0004	0.0669	0.0111
J1932+1059	59062	375	0.0352	0.0007	0.0285	0.0008	0.1331	0.0219
J1932+1059	59062	425	0.0347	0.0005	0.0293	0.0004	-0.0326	0.0256
J1932+1059	59062	475	0.0345	0.0007	0.0278	0.0006	-0.1200	0.0297
J1932+1059	59062	575	0.0337	0.0007	0.0303	0.0004	—	—
J1932+1059	59062	625	0.0332	0.0004	0.0323	0.0004	-0.0221	0.0095
J1932+1059	59062	675	0.0350	0.0006	0.0356	0.0006	-0.0221	0.0095
J1932+1059	59062	725	0.0297	0.0005	0.0304	0.0006	-0.0192	0.0152
J1932+1059	59497	325	0.0365	0.0008	0.0279	0.0009	-0.8215	0.0090
J1932+1059	59497	375	0.0351	0.0007	0.0294	0.0004	0.1062	0.0302
J1932+1059	59497	425	0.0399	0.0004	0.0320	0.0005	0.1479	0.0287
J1932+1059	59497	475	0.0389	0.0007	0.0341	0.0008	0.2495	0.3407
J1932+1059	59497	575	0.0405	0.0016	0.0363	0.0012	—	—
J1932+1059	59497	625	0.0393	0.0014	0.0358	0.0013	-0.0815	0.0392
J1932+1059	59497	675	0.0433	0.0017	0.0385	0.0012	-0.0222	0.0103
J1932+1059	59497	725	0.0461	0.0022	0.0416	0.0013	—	—
J2048-1616	59062	325	0.0221	0.0006	0.0108	0.0009	-0.4158	0.0081
J2048-1616	59062	375	0.0198	0.0007	0.0113	0.0023	-0.0211	0.0077
J2048-1616	59062	425	0.0247	0.0020	0.0108	0.0012	-0.1529	0.0139
J2048-1616	59062	625	0.0152	0.0004	0.0132	0.0005	-0.0058	0.0012
J2048-1616	59062	675	0.0152	0.0004	0.0138	0.0005	0.0208	0.0090
J2048-1616	59062	725	0.0148	0.0004	0.0135	0.0005	0.00005	0.0001

NOTE—Scintillation arc measurements and drift rates in the left and right primary arms of each epoch at all frequencies where measurable. η_L and η_R are the the arc curvature measurements for the left and right arms, respectively, and $d\nu/dt$ is the measured scintillation drift rate, with the matching σ 's representing the corresponding uncertainties. All curvatures and their errors have been scaled to 1 GHz and errors on curvature here are fit uncertainties. Some pulsars on MJD 59497 have multiple curvature measurements at a given frequency, due to this epoch being 155 minutes instead of the 40 minutes of the other observations, and so a new η was measured after every 40 minutes.

4.1. Scintillation Arc Curvature Scaling Behavior

As mentioned earlier, Hill et al. (2003) demonstrated through both theoretical and observational means that the arc curvature η should follow a ν^{-2} dependence, implying that scattering is dominated by one or several thin screens along the LOS. While over 2 GHz of bandwidth was used in those observations (10-12.5 MHz of bandwidth centered at 430 MHz and either 50 or 100 MHz of bandwidth centered at 1175 MHz, 1400 MHz, and 2250 MHz), the frequency coverage was discontinuous and all η measurements used in their corresponding fits were from different epochs. Generally the latter point should not be an issue as long as the observations were taken within a period shorter than the pulsar's refractive timescale. Indeed, for the data used in their fits, their measured arc curvatures at a given frequency did not vary

significantly on day or week timescales, making them suitable for this type of analysis. However, the ideal situation would be to obtain many measurements at many frequencies during the same observation, preferably at the same time for optimal consistency. With our high resolution and sufficient observing time, we have the ability to make up to eight concurrent arc measurements over 450 MHz of bandwidth at low frequency and can consequentially provide a more definitive examination of the theory.

Following the methodology of Hill et al. (2003), for a scaling index α , we performed a weighted linear least-squares fit of the form

$$\log_{10} \eta = \alpha \log_{10} \nu + \beta \quad (3)$$

on the unscaled curvatures for each pulsar at each MJD. Example fits can be seen in Figure 1, with all measured in-

dices listed in Table 2. We find that, overall, our scaling indices are consistent with a theoretical index of -2 , which assumes thin screen scattering (Stinebring et al. 2001), with PSRs J1136+1551 and J1932+1059 being especially consistent. This effect can also be seen in Table 1, where arc curvatures at all frequencies from a given pulsar at the same MJD are generally in strong agreement after being scaled to 1 GHz. Interestingly, a weighted average of all curvature fits shows that our left arm fits are overall more consistent with an index of -2 than our right arms, with a weighted average of -1.99 ± 0.03 across all left arm fits compared with -1.69 ± 0.02 across all right arm fits, indicating that refraction may play a role in how closely arc curvature scales as expected with frequency.

4.2. Scattering Delay Scaling Behavior

Our wide frequency coverage also allowed us to examine the scaling index of scattering delays. Under the assumption that ISM fluctuations follow behaviors consistent with a Kolmogorov medium and that scattering can be modeled as the result of interactions of pulsar emission with an infinite, thin, scattering screen during its propagation, we should expect that scattering delays scale with frequency as $\tau_d \propto \nu^{-4.4}$ (Romani et al. 1986; Cordes & Rickett 1998). Previous studies examining the scattering indices of various pulsars have done so using a number of methods, including simultaneous multi-frequency measurements (Bhat et al. 2004; Bansal et al. 2019), splitting up measurements from a single frequency band into multiple subbands (Levin et al. 2016; Turner et al. 2021), and using measurements from many epochs taken at two observing bands non-simultaneously (Turner et al. 2021). Since more measurements and more frequency coverage in a single epoch is ideal, the method used in Bhat et al. (2004) and Bansal et al. (2019) is the most preferred of the three. The method in this paper utilizes a combination of this approach and the subband approach to maximize the number of delay measurements per epoch, which can be done thanks to our high frequency resolution and sensitivity in both observing bands.

Similar to Equation 3 used to determine the arc curvature scaling index, our scattering delay scaling indices ξ at each epoch were determined by performing a weighted linear least-squares fit of the form

$$\log_{10} \tau_d = \xi \log_{10} \nu + b. \quad (4)$$

Example fits can be seen in Figure 2, with all measured indices listed in Table 3. We find that half of our measured indices are consistent with a Kolmogorov medium, while the other half are consistent with a shallower medium. This behavior agrees well with previous studies, as both Bhat et al. (2004) and Bansal et al. (2019) found indices either consistent with a Kolmogorov medium or shallower than a Kolmogorov medium, while Levin et al. (2016) and Turner et al.

(2021) only found indices that were shallower than a Kolmogorov medium.

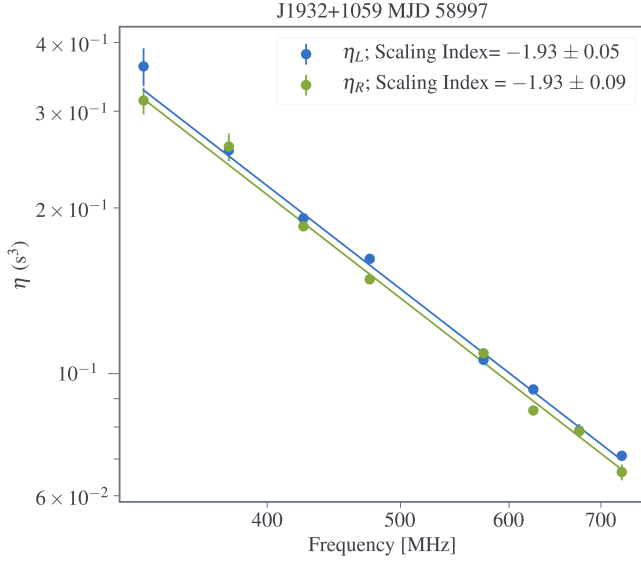
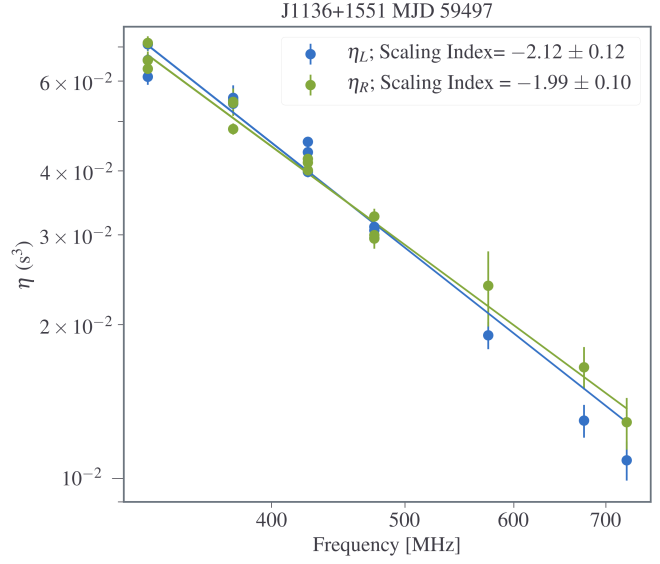
Many explanations have been given for why shallower-than-Kolmogorov medium behavior has been observed so frequently. Physical arguments have called into question the validity of the simple infinite, thin screen model, demonstrating that shallower scaling indices are more consistent with finite, thin screens (Rickett et al. 2009). This is expected to be much more common among low DM pulsars (Cordes & Lazio 2001), which agrees with our results, as all of the pulsars have dispersion measures below 40 pc cm^{-3} . Shallower indices have also been attributed to the existence of multiple finite screens along the LOS (Lewandowski et al. 2013). This hypothesis agrees well with our measured indices for PSR B1133+16, as its indices are consistently shallower than that of a Kolmogorov medium and it is also known to have at least six distinct scattering screens (McKee et al. 2022).

Quality-of-data arguments have also been proposed. Turner et al. (2021) suggested their shallower indices may be at least partially attributable to an imbalance of lower frequency data to higher frequency data for their multiple epoch approach as well as a lack of sufficient frequency resolution in their lower frequency band in some epochs. However, neither of these issues should affect our results, as our observations have a consistently even balance of low and high frequency measurements at all epochs and all of our measurements are well-resolved in frequency.

4.3. 155 Minute Observation

The inclusion of a 155 minute observation in our survey on MJD 59497 allowed for an analysis of short-term arc curvature variation in some pulsars, as observations had to be paused every 40 minutes for a five minute phase calibration, resulting in multiple 40 minute sub-observations. For pulsars with at least two measurements in a given scintillation arc at a given frequency, we examined overall variation in that arc at that frequency by looking at the percent difference between a given curvature measurement and the weighted average curvature for that arm and frequency over the entire epoch.

For PSR J1136+1551, all observing frequencies centered at or below 475 MHz had three measurements in each primary arm (the brightest arm, overwhelmingly often the arm with the lowest curvature) at each frequency, with the accumulation of all percent differences yielding a bimodal distribution with peaks around percent differences of 2% and 7%. The largest percent difference away from a weighted mean was $7.9 \pm 0.2\%$ and the smallest was $0.14 \pm 1.91\%$, although the majority of all percent differences was below 3%. All of this strongly indicates the ISM underwent very little change along the LOS to this pulsar over the course of a given observation. This result is supported by this pulsar’s incredibly low dispersion measure, meaning it does not sample a size-

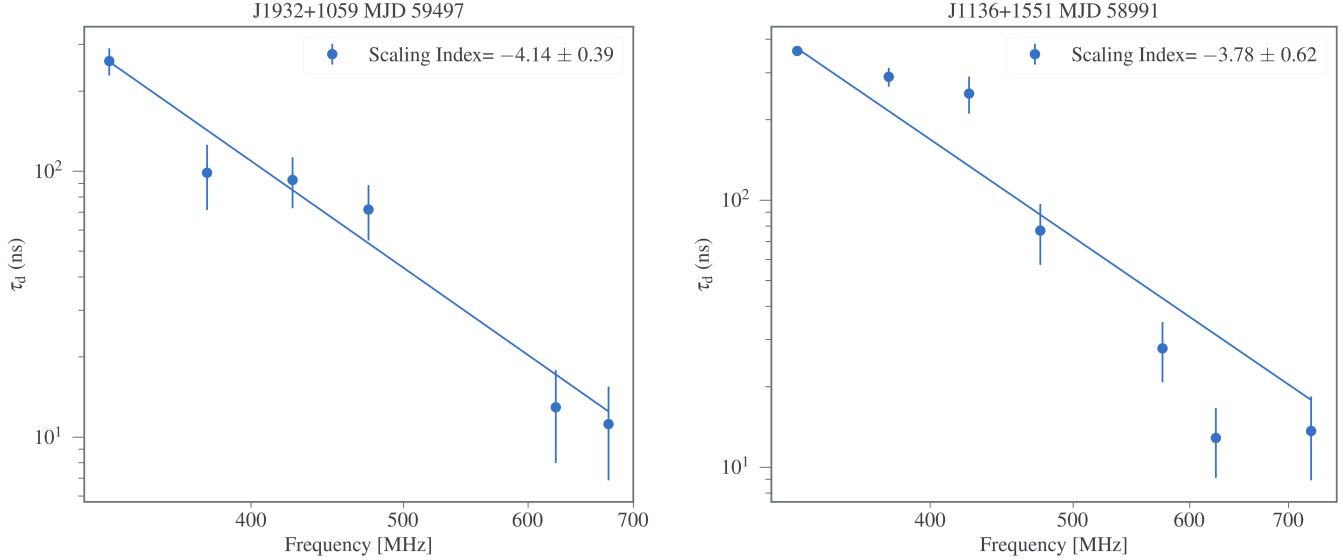
(a) α fit for PSR J1932+1059 on MJD 58997(b) α fit for PSR J1136+1551 on MJD 59497. The inclusion of multiple points at certain frequencies is the result of this epoch containing a 155 minute observation instead of the 40 minutes of the other observations, and so a new η was measured after every 40 minutes.**Figure 1.** Example fits for the arc curvature scaling index**Table 2.** Fitted Pulsar Scintillation Arc Curvature Scaling Indices

Pulsar	MJD	Scaling Index Left Arc	Scaling Index Error Left Arc	N_η	Scaling Index Right Arc	Scaling Index Error Right Arc	N_η
J0630–2834	58987	—	—	—	–2.48	0.31	8
J1136+1551	58987	–1.79	0.11	7	–1.89	0.12	7
J1136+1551	58991	–1.65	0.12	8	–1.94	0.08	8
J1136+1551	59115	–1.36	0.13	8	–1.52	0.15	8
J1136+1551	59497	–2.12	0.12	15	–1.99	0.10	15
J1509+5531	58987	–1.49	0.83	3	–1.34	0.55	3
J1509+5531	59064	–1.62	0.26	4	–1.41	0.22	4
J1509+5531	59115	–0.93	0.21	4	–2.31	0.18	4
J1509+5531	59497	–2.01	0.87	9	–1.34	0.21	9
J1645–0317	59074	–2.09	0.26	4	—	—	—
J1932+1059	58997	–1.93	0.05	8	–1.93	0.09	8
J1932+1059	59062	–2.08	0.07	8	–1.75	0.07	8
J1932+1059	59497	–1.77	0.09	8	–1.53	0.04	8
J2048–1616	59062	–2.52	0.07	6	–1.68	0.05	6

NOTE—Fitted arc curvature scaling indices for both left and right primary arcs. N_η indicates the number of arc curvature measurements used in each fit. Measurements on MJD 59497 may have $N_\eta > 8$ due to this epoch being 155 minutes rather than the 40 minutes of the other observations, and so a new η was measured after every 40 minutes. Arc curvature measurements used in these fits were left unscaled.

able portion of the ISM along its LOS relative to many pulsars that are observed (Bilous et al. 2016; Manchester et al. 2005; Pilkington et al. 1968).

For PSR J1509+5531, all observing frequencies centered at or above 575 MHz had at least two measurements in each arm at each frequency, with the accumulation of all percent differences resulting in a one-sided distribution peaked



(a) Scattering delay scaling index fit for PSR J1932+1059 on MJD 59497

(b) Scattering delay scaling index fit for PSR J1136+1551 on MJD 58991.

Figure 2. Example fits for the scattering delay scaling index**Table 3.** Fitted Pulsar Scattering Delay Scaling Indices

Pulsar	MJD	Scaling Index	Index Error	N_{τ_d}
J0630–2834	58987	−4.19	1.43	8
J1136+1551	58987	−1.44	0.71	6
J1136+1551	58991	−3.78	0.62	7
J1136+1551	59115	−2.72	1.05	6
J1136+1551	59497	−1.71	0.57	13
J1645–0317	59074	−4.60	0.75	4
J1932+1059	58997	−1.83	0.31	7
J1932+1059	59062	−1.74	0.31	6
J1932+1059	59497	−4.14	0.39	6
J2048–1616	59062	−3.77	1.39	6

NOTE—Fitted scattering delay scaling indices, with a minimum of four delay measurements (N_{τ_d}) required in a given epoch to obtain a scaling index. Errors are the parameter uncertainties from parameter fits. Half of our measured indices were consistent with a Kolmogorov medium, while the other half were consistent with a shallower medium. Measurements on MJD 59497 may have $N_{\tau_d} > 8$ due to this epoch being 155 minutes rather than the 40 minutes of the other observations, and so a new η was measured after every 40 minutes.

around 6%. The smallest percent difference away from a weighted mean was $1.2 \pm 2.1\%$, while the largest was $36 \pm 0.1\%$, although the next largest after that was only $22 \pm 0.1\%$, meaning this maximum was an extreme outlier. The majority of all percent differences was below 7%. As with the previous pulsar, this also strongly indicates the ISM

underwent very little change along the LOS to this pulsar over the course of a given observation, a result again supported by this pulsar’s fairly low dispersion measure (Huguenin et al. 1968; Manchester et al. 2005). The fact that this pulsar shows higher variation of this observation compared to PSR J1136+1551 is likely due to PSR J1509+5531 having a dispersion measure four times higher and a transverse velocity 45% larger (Bilous et al. 2016; Huguenin et al. 1968; Manchester et al. 2005; Pilkington et al. 1968; Stovall et al. 2015), so a significantly larger fraction of the ISM was sampled during its observation, increasing the likelihood of larger scintillation-based variations.

The next few subsections will be dedicated to highlighting the features of a few pulsars in the survey.

4.4. J0630-2834

In the one epoch for which we were able to resolve a scintillation arc, only the right arm was resolvable across all frequencies, with its relative brightness relative to the left side of the fringe frequency axis consistently decreasing as frequency increased. An example of this asymmetry can be seen in Figure 3. This strong asymmetry is known to be the result of refraction leading to scintillation drifting in the dynamic spectra (Cordes et al. 2006). Interestingly, despite our asymmetry appearing to decrease with frequency, the magnitude of our measured scintillation drift rates seem to mildly favor an increase with frequency, whereas one would expect an increase in scintillation drift to coincide with an increase in the asymmetry.

4.5. J1136+1551

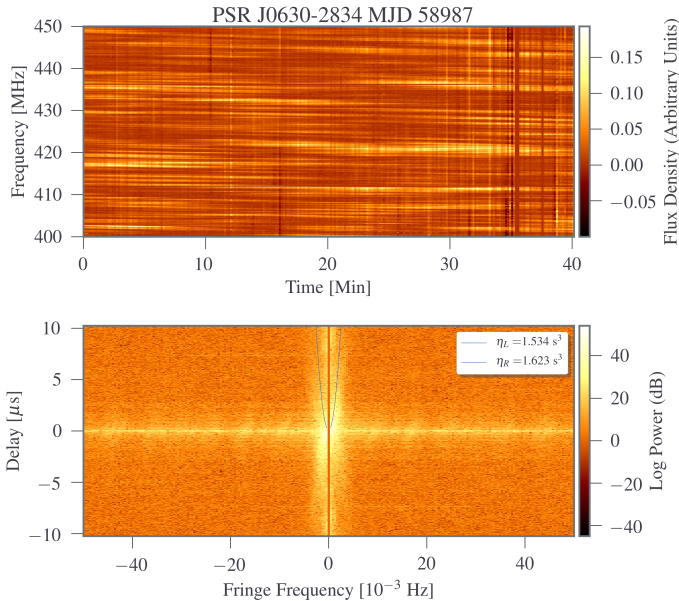


Figure 3. An example dynamic (top) and secondary (bottom) spectrum from PSR J0630-2834 on MJD 58987 centered at 425 MHz. There is a clear asymmetry in the secondary spectrum, with the right arm being the dominant feature. This is likely the result of refraction along the line of sight. The green line represents the arc curvature fit and the arc curvature measurement quoted is unscaled. Scaled uncertainties of the arc curvature can be found in Table 1.

This pulsar is well known for having the uncommon feature of multiple scintillation arcs, implying multiple scattering screens along its LOS (Hill et al. 2003; Stinebring et al. 2019). In the literature six distinct sets of arcs have been found over a ~ 34 year span of observations (McKee et al. 2022). In three of the four epochs in which we observed this pulsar, we observed multiple arcs, an example of which can be seen in Figure 4. After scaling our measurements to 1400 MHz and using the convention from McKee et al. (2022), we can conclude that we detected arcs E, C, and B on MJDs 58987 and 58991 and arcs D and C on MJD 59115, with arc C being the only detectable arc on MJD 59497. All multiple-arc detections were made only in the observations using uGMRT’s band 4, which was centered at 650 MHz. The fact that the two epochs closest to each other in our survey (58987 and 58991) both detected the same sets of arcs may hint at a timescale over which certain screens have a larger influence over the pulsar signal propagation.

An examination of the power in each of the arms show notable levels of asymmetry along the delay axis, and consequently a notable amount of refraction, in all detectable arms and across all frequencies in the first two epochs, with the right arm having more power and extending further out on the delay axis. This asymmetry clearly decreases over the course of our observations across all frequencies until our final observation, where the arcs have approximately even levels of

power or the left arc starts to dominate in the asymmetry. This trend is generally supported by the measured scintillation drift rates as well, especially for data taken at band 4 (650 MHz), i.e., the same band where the multiple arcs were visible, as measured drifts are generally positive during the first three epochs and then considerably negative during the final epoch.

Perhaps the most interesting finding from our observations of this pulsar is the discovery of a strong correlation between the measured arc curvatures and the arc asymmetry index, which is a metric that describes the relative power between the left and right arcs and is found by comparing the average power along each arc via

$$A = \frac{\overline{P_R(f_\nu)} - \overline{P_L(f_\nu)}}{\overline{P_R(f_\nu)} + \overline{P_L(f_\nu)}}, \quad (5)$$

with a larger index magnitude indicating greater asymmetry. We believe this phenomenon has never before been reported and is therefore worth further examination in future observations. As briefly mentioned earlier, asymmetry in arcs has long been attributed to either the refraction of pulsar emission at the scattering screen or as the result of an asymmetric distribution of the material within the screen (Cordes et al. 2006), while arc curvature is known to indicate the distance between a given scattering screen and the observer (Stinebring et al. 2001). The correlation between the two suggests further study of this effect may result in a better understanding of how screen asymmetry and/or refraction affects pulsar emission depending on the scattering screen’s proximity to the pulsar.

An example dynamic and secondary spectrum pair is shown in Figure 5, with its corresponding normalized secondary spectrum power profile, which is used to determine the asymmetry index, shown in Figure 6, while the scatter plot showing the relation between measured arc curvature and arc asymmetry index across all measurements taken in the 650 MHz band is shown in Figure 7. Of particular note in Figure 7 are the three distinct clumps, which we believe are the result of our observations being dominated by a different scattering screen at each epoch (two of our observations were taken four days apart, and so are dominated by the same screen). It is likely that this pulsar’s at least six known scattering screens are the main reason why we were able to see this correlation in our data in the first place, as individual scattering screens likely do not vary enough in distance over time for this trend to become apparent. Indeed, the limited number of pulsars with multiple known screens is probably the main reason why this trend has not been reported in earlier studies.

4.6. J1509+5531

In the observations of this pulsar in the 650 MHz band, all secondary spectra featured patchy rather than continuous

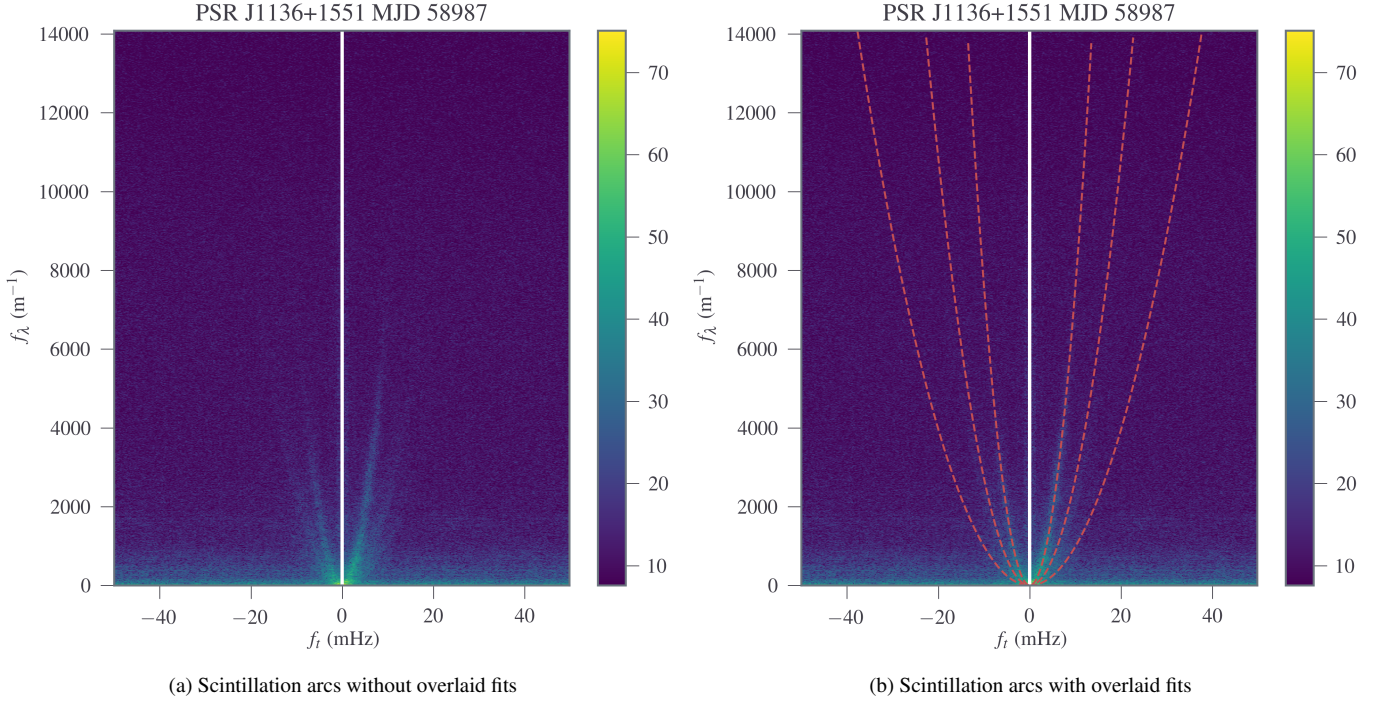


Figure 4. Secondary spectrum of PSR J1136+1551 at 650 MHz on MJD 58987 showing the detection of three distinct scintillation arcs.

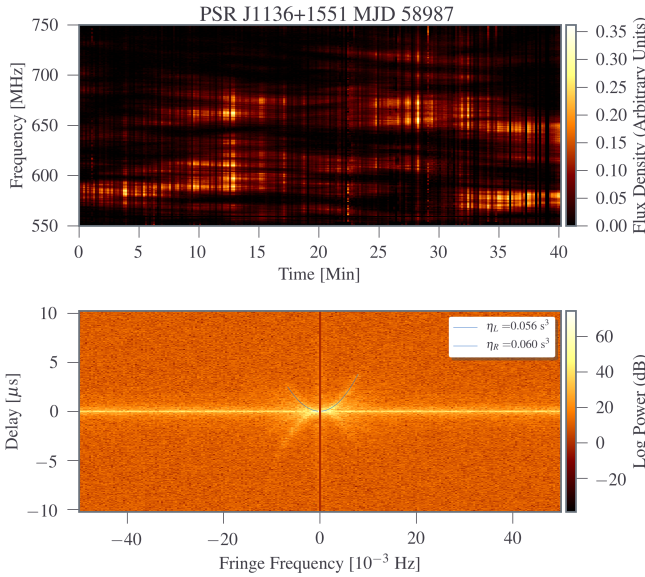


Figure 5. Dynamic (top) and secondary (bottom) spectra of PSR J1136+1551 centered at 650 MHz on MJD 58987. The top half of the secondary spectrum shows the overlaid arc fits in green. Scaled uncertainties of the arc curvature can be found in Table 1.

arcs, particularly in the left arm. This patchiness indicates a detection of this pulsar’s arcllets, which result from substructures in the ISM thought to arise from scattering interference between an inhomogenously scattered distribution of material and some distinct offset region (Walker & Stinebring 2005; Cordes et al. 2006). In the particular case of this

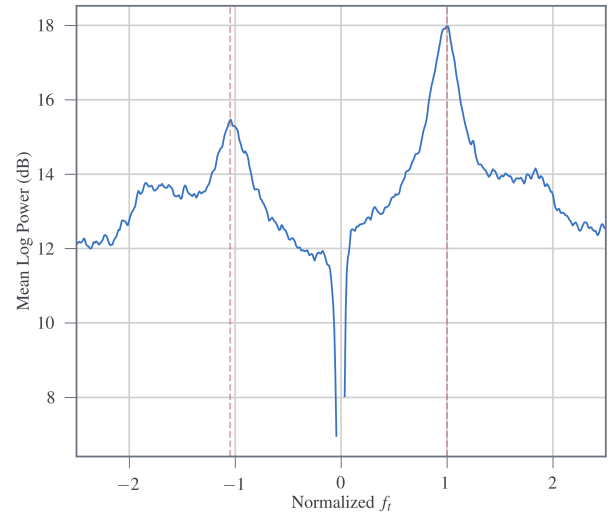


Figure 6. Normalized secondary spectrum power profile of PSR J1136+1551 centered at 650 MHz on MJD 58987. The vertical dashed lines indicate where the arcs fall on the normalized delay axis.

pulsar these substructures are roughly AU in scale. Unique to these arcllets is their distinctly flat nature, which has been attributed to its exceptionally high transverse velocity of over 960 km s^{-1} (Manchester et al. 2005). Interestingly, the arc curvatures measured in the last two epochs (MJDs 59115 and 59497) are a factor of two to three times smaller than the first

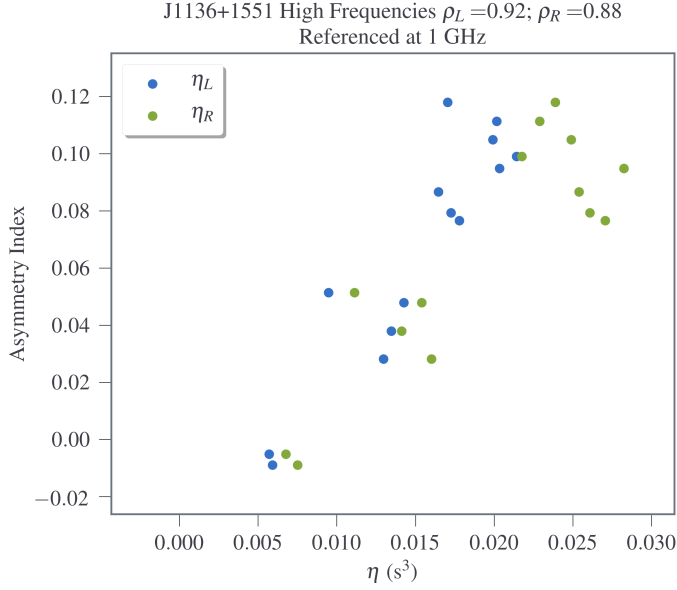


Figure 7. Scatter plot showing measured arc curvatures and the corresponding asymmetry indices for all measurements of PSR J1136+1551 taken with Band 4. All arc curvatures have been scaled to their corresponding 1 GHz equivalent. The three distinct clumps are the result of the observations being dominated by three different scattering screens.

two epochs (MJDs 59064 and 58987), possibly indicating a detection of multiple scattering screens along the LOS to this pulsar. This result augments the results of [Sprenger et al. \(2022\)](#), who also found significant variability along the LOS to this pulsar during the same period of time. An example observation from the earlier two epochs is shown in [Figure 8](#), while an example from the later two epochs is shown in [Figure 9](#).

4.7. J1932+1059

Due to having the lowest DM in our survey, this pulsar showed the least variation in arc curvature from epoch to epoch across all frequencies. Its close proximity to Earth also resulted in wide scintles in frequency, leading to high scintle resolution and, consequently, very bright, narrow, and well defined arcs. The sharpness of these arcs may also indicate scattering that is highly anisotropic along the LOS ([Walker et al. 2004](#); [Cordes et al. 2006](#)), as well as originating from a discrete, localized source ([Stinebring et al. 2001](#)). Overall this was our most consistent pulsar in all aspects of scintillation.

This consistency lines up with its other astrophysical parameters, as its dispersion measure of 3.18 pc cm^{-3} ([Large et al. 1968](#); [Manchester et al. 2005](#)) was the lowest in our survey and its transverse velocity of 152 km s^{-1} ([Bilous et al. 2016](#); [Manchester et al. 2005](#)) was the second lowest. While its transverse velocity is a bit larger than PSR

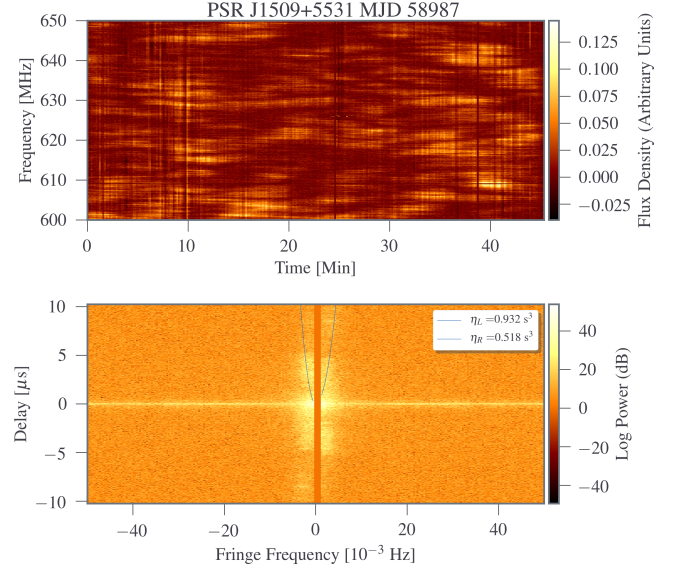


Figure 8. Dynamic (top) and secondary (bottom) spectra of PSR J1509+5531 centered at 625 MHz on MJD 58987. The top half of the secondary spectrum shows the overlaid arc fits in green. Scaled uncertainties of the arc curvature can be found in [Table 1](#). During this period of observations, visible arcs were considerably narrower than later observations.

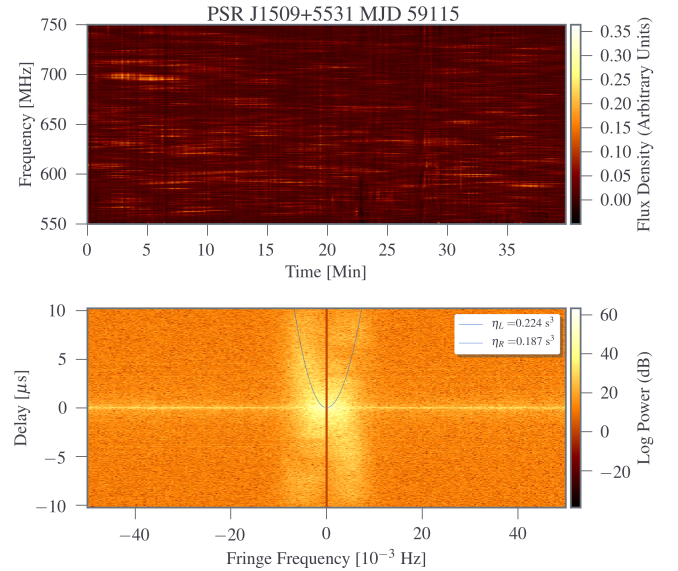


Figure 9. Dynamic (top) and secondary (bottom) spectra of PSR J1509+5531 centered at 650 MHz on MJD 59115. The top half of the secondary spectrum shows the overlaid arc fits in green. Scaled uncertainties of the arc curvature can be found in [Table 1](#). During this period of observations, visible arcs were considerably wider than later observations.

J0630–2834 and their distances are almost equivalent, PSR J0630–2834 has a dispersion measure 10 times higher than PSR J1932+1059 ([Large et al. 1968, 1969](#); [Manchester et al.](#)

2005). This means that a much denser ISM was sampled in PSR J0630–2834 than in PSR J1932+1059, meaning that PSR J1932+1059 had decisively the least amount of ISM sampled over our survey, making it the least likely to experience large scintillation-related variations. An example observation is shown in Figure 10.

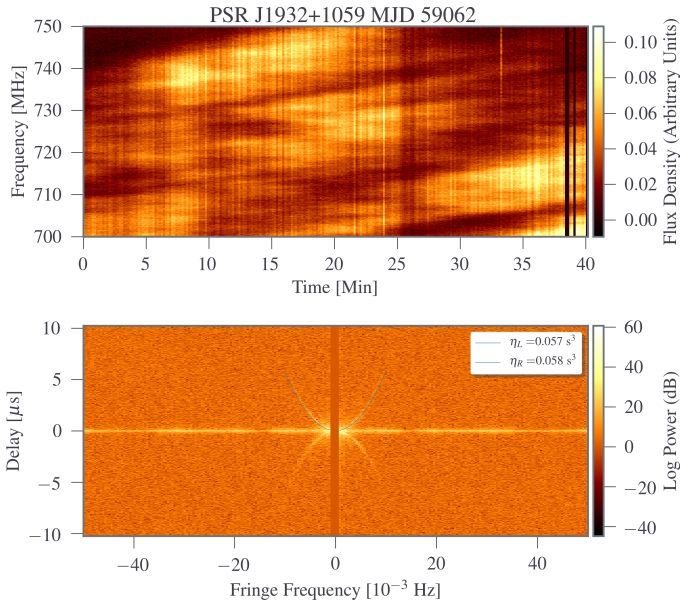


Figure 10. Dynamic (top) and secondary (bottom) spectra of PSR J1932+1059 centered at 725 MHz on MJD 58987. The top half of the secondary spectrum shows the overlaid arc fits in green. Scaled uncertainties of the arc curvature can be found in Table 1.

5. CONCLUSIONS & FUTURE WORK

We performed simultaneous dual-frequency observations of six bright canonical pulsars using the uGMRT. We extracted scintillation arc, bandwidth, and drift rate measure-

ments for each of these pulsars to examine a variety of science. We examined how arc curvature scaled with frequency and found our observations to be consistent with the index predicted by theory, while at the same time using a more astronomically ideal setup to perform these measurements. We also measured scattering delay scaling indices for five of our six pulsars and found indices consistent with or shallower than what is expected from a Kolmogorov medium, agreeing with previous literature. Finally, we find an interesting and strong correlation between arc curvature and arc asymmetry in PSR J1136+1551, demonstrating a potential connection between screen asymmetry and/or refraction and scattering screen location along the LOS, and the which we intend to follow up with additional observations.

This study demonstrates the value of array-based telescopes such as uGMRT to the pulsar astronomy community, as well as the strengths of simultaneous multiband studies of pulsars and the wide variety of science that can be done with such an approach. This also shows strong promise for the future observations using ultrawideband (UWB) receivers, which are coming online at instruments such as the Green Bank Telescope.

We thank the staff at the uGMRT who have made these observations possible. The uGMRT is run by the National Centre for Radio Astrophysics of the Tata Institute of Fundamental Research. We gratefully acknowledge support of this effort from the NSF Physics Frontiers Center grants 1430284 and 2020265 to NANOGrav. Some of the data processing in this work utilized the resources of the Bowser computing cluster at West Virginia University.

Software: SCINTOOLS Reardon et al. (2020), PYPULSE Lam (2017), SCIPY Virtanen et al. (2020), NUMPY van der Walt et al. (2011), and MATPLOTLIB Hunter (2007).

REFERENCES

- Bansal, K., Taylor, G. B., Stovall, K., & Dowell, J. 2019, *The Astrophysical Journal*, 875, 146, doi: [10.3847/1538-4357/ab0d8f](https://doi.org/10.3847/1538-4357/ab0d8f)
- Bhat, N. D. R., Cordes, J. M., Camilo, F., Nice, D. J., & Lorimer, D. R. 2004, *The Astrophysical Journal*, 605, 759, doi: [10.1086/382680](https://doi.org/10.1086/382680)
- Bilous, A. V., Kondratiev, V. I., Kramer, M., et al. 2016, *A&A*, 591, A134, doi: [10.1051/0004-6361/201527702](https://doi.org/10.1051/0004-6361/201527702)
- Cordes, J. M., & Lazio, T. J. W. 2001, *The Astrophysical Journal*, 549, 997, doi: [10.1086/319442](https://doi.org/10.1086/319442)
- Cordes, J. M., & Rickett, B. J. 1998, *The Astrophysical Journal*, 507, 846, doi: [10.1086/306358](https://doi.org/10.1086/306358)
- Cordes, J. M., Rickett, B. J., Stinebring, D. R., & Coles, W. A. 2006, *ApJ*, 637, 346, doi: [10.1086/498332](https://doi.org/10.1086/498332)
- Hill, A. S., Stinebring, D. R., Barnor, H. A., Berwick, D. E., & Webber, A. B. 2003, *The Astrophysical Journal*, 599, 457, doi: [10.1086/379191](https://doi.org/10.1086/379191)
- Huguenin, G. R., Taylor, J. H., Goad, L. E., et al. 1968, *Nature*, 219, 576, doi: [10.1038/219576a0](https://doi.org/10.1038/219576a0)
- Hunter, J. D. 2007, *Computing in Science & Engineering*, 9, 90, doi: [10.1109/MCSE.2007.55](https://doi.org/10.1109/MCSE.2007.55)
- Lam, M. T. 2017, *PyPulse: PSRFITS handler*. <http://ascl.net/1706.011>
- Large, M. I., Vaughan, A. E., & Wielebinski, R. 1968, *Nature*, 220, 753, doi: [10.1038/220753a0](https://doi.org/10.1038/220753a0)
- . 1969, *Nature*, 223, 1249, doi: [10.1038/2231249a0](https://doi.org/10.1038/2231249a0)

- Levin, L., McLaughlin, M. A., Jones, G., et al. 2016, *The Astrophysical Journal*, 818, 166.
<http://stacks.iop.org/0004-637X/818/i=2/a=166>
- Lewandowski, W., Dembska, M., Kijak, J., & Kowalińska, M. 2013, *Monthly Notices of the Royal Astronomical Society*, 434, 69, doi: [10.1093/mnras/stt989](https://doi.org/10.1093/mnras/stt989)
- Manchester, R. N., Hobbs, G. B., Teoh, A., & Hobbs, M. 2005, *AJ*, 129, 1993, doi: [10.1086/428488](https://doi.org/10.1086/428488)
- McKee, J. W., Zhu, H., Stinebring, D. R., & Cordes, J. M. 2022, *The Astrophysical Journal*, 927, 99, doi: [10.3847/1538-4357/ac460b](https://doi.org/10.3847/1538-4357/ac460b)
- Pilkington, J. D. H., Hewish, A., Bell, S. J., & Cole, T. W. 1968, *Nature*, 218, 126, doi: [10.1038/218126a0](https://doi.org/10.1038/218126a0)
- Reardon, D. J., Coles, W. A., Bailes, M., et al. 2020, *ApJ*, 904, 104, doi: [10.3847/1538-4357/abbd40](https://doi.org/10.3847/1538-4357/abbd40)
- Rickett, B., Johnston, S., Tomlinson, T., & Reynolds, J. 2009, *Monthly Notices of the Royal Astronomical Society*, 395, 1391, doi: [10.1111/j.1365-2966.2009.14471.x](https://doi.org/10.1111/j.1365-2966.2009.14471.x)
- Romani, R. W., Narayan, R., & Blandford, R. 1986, *MNRAS*, 220, 19, doi: [10.1093/mnras/220.1.19](https://doi.org/10.1093/mnras/220.1.19)
- Sprenger, T., Main, R., Wucknitz, O., Mall, G., & Wu, J. 2022, *Monthly Notices of the Royal Astronomical Society*, 515, 6198, doi: [10.1093/mnras/stac2160](https://doi.org/10.1093/mnras/stac2160)
- Stinebring, D. R., McLaughlin, M. A., Cordes, J. M., et al. 2001, *ApJL*, 549, L97, doi: [10.1086/319133](https://doi.org/10.1086/319133)
- Stinebring, D. R., Rickett, B. J., & Ocker, S. K. 2019, *ApJ*, 870, 82, doi: [10.3847/1538-4357/aaef80](https://doi.org/10.3847/1538-4357/aaef80)
- Stinebring, D. R., Rickett, B. J., Minter, A. H., et al. 2022, *The Astrophysical Journal*, 941, 34, doi: [10.3847/1538-4357/ac8ea8](https://doi.org/10.3847/1538-4357/ac8ea8)
- Stovall, K., Ray, P. S., Blythe, J., et al. 2015, *The Astrophysical Journal*, 808, 156, doi: [10.1088/0004-637x/808/2/156](https://doi.org/10.1088/0004-637x/808/2/156)
- Trang, F. S., & Rickett, B. J. 2007, *ApJ*, 661, 1064, doi: [10.1086/516706](https://doi.org/10.1086/516706)
- Turner, J. E., McLaughlin, M. A., Cordes, J. M., et al. 2021, *ApJ*, 917, 10, doi: [10.3847/1538-4357/abfafe](https://doi.org/10.3847/1538-4357/abfafe)
- van der Walt, S., Colbert, S. C., & Varoquaux, G. 2011, *Computing in Science Engineering*, 13, 22
- Virtanen, P., Gommers, R., Oliphant, T. E., et al. 2020, *Nature Methods*, 17, 261, doi: <https://doi.org/10.1038/s41592-019-0686-2>
- Walker, M. A., Melrose, D. B., Stinebring, D. R., & Zhang, C. M. 2004, *MNRAS*, 354, 43, doi: [10.1111/j.1365-2966.2004.08159.x](https://doi.org/10.1111/j.1365-2966.2004.08159.x)
- Walker, M. A., & Stinebring, D. R. 2005, *MNRAS*, 362, 1279, doi: [10.1111/j.1365-2966.2005.09396.x](https://doi.org/10.1111/j.1365-2966.2005.09396.x)